UNIVERSITY *of York*

This is a repository copy of *A Pulse Antenna Suite for IEMI Testing*.

White Rose Research Online URL for this paper:
https://eprints.whiterose.ac.uk/215734/

Version: Accepted Version

Article:

White Rose

university consortium
Universities of Leeds, Sheffield & York

eprints@whiterose.ac.uk
https://eprints.whiterose.ac.uk/

A Pulse Antenna Suite for IEMI Testing

John F. Dawson, *Member, IEEE*, Simon J. Bale, Martin P. Robinson, Tim Rees, Barnabas J. Petit, Richard Hoad and Mark Hough

Abstract—**This article describes the development and testing of a suite of high-voltage pulse antennas for IEMI susceptibility testing. The antennas are designed to operate with pulses up to 33 kV from a common solid state double exponential pulse generator, and to be light enough to operate on a standard EMC test mast. A broadband (hyperband) antenna intended to transmit the full pulse spectrum and two resonant (mesoband) antennas to produce damped sinusoidal pulses are presented. The antennas were prototyped using full wave numerical modelling and tested in an anechoic chamber in the frequency domain and with a high voltage pulse generator.**

Index Terms—**Intentional Electromagnetic Interference, Pulse Antenna, Antenna Design**

I. INTRODUCTION

S EVERAL published standards [1], [2], and [3] indicate that a wide variety of Intentional Electromagnetic Interference (IEMI) sources are available which produce pulsed interference. These sources could pose a potential threat to a wide range of equipment and systems including Critical National Infrastructure (CNI) [4] and [5].

When assessing the risk from these IEMI sources to CNI [4] one must either;

a) assume an immunity level, based on EMC limits or sparse effects data, which will likely have an inherent high degree of uncertainty; or

b) conduct an immunity test on actual or representative equipment with an actual or representative simulation of threat sources.

For case b) above, an immunity test capability is required. A radiated IEMI immunity test capability has been developed at QinetiQ in the UK using a solid state pulser with very good pulse to pulse stability.

A range of antennas suitable for IEMI applications have been discussed in the literature [6]–[12]. In this paper we present a lightweight, compact, robust, high voltage planar Vivaldi antenna which, working with a pulsed source, provides Hyperband (broadband) pulsed fields and can be accommodated on a typical EMC test mast, along with two dipole antennas designed to produce a damped sinusoidal (Mesoband) field with the same pulsed source. In Section II we summarise the antenna requirements for IEMI testing. In

Section III we compare possible candidate Hyperband antennas, and present initial performance estimates. The design of two mesoband antennas is then described in Sections V and IV. The measurement setup and data processing for performance evaluation of the antennas is summarised in Section VII and a comparison of modelled and measured performance is presented in Section VIII.

II. ANTENNA REQUIREMENTS

The antennas are intended to work with a single pulse generator [13] having a double exponential waveform with a rise-time of about 90 ps and full width half-height (FWHH) of about 2.5 ns. We have used a unit double exponential pulse of the form:

$$v(t) = k(e^{-At} - e^{-Bt}), \qquad (1)$$

[14], where $k = 1.0649$, $A = 2.773 \times 10^8 \ s^{-1}$, and $B = 2.4414 \times 10^{10} \ s^{-1}$, scaled to the appropriate peak value, to represent the pulse generator output in the simulated results. The pulse generator has a nominal output of up to 24 kV with a +3 dB tolerance, meaning that it may generate pulses of up to approximately 34 kV. The pulse parameters were obtained by fitting (1) to the measured pulse obtained in earlier work as shown in Fig. 1.
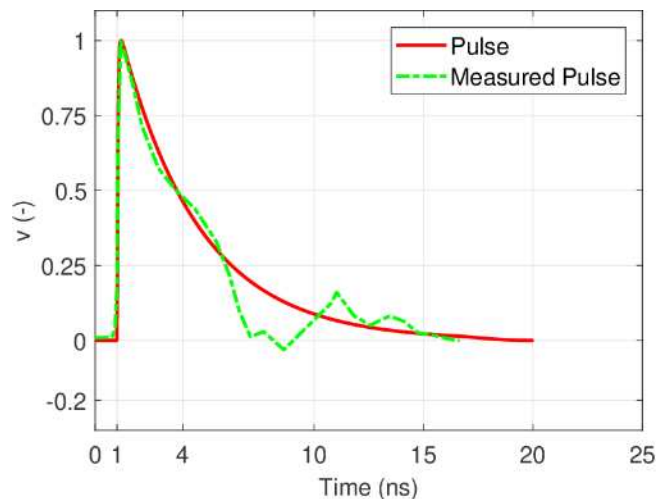
Fig. 1 Comparing measured and ideal unit pulse (3 ns FWHH double exponential pulse with 90 ps rise time)

It is desirable that the amplitude of the radiated pulse is as uniform as possible over a defined test region. Here we

considered a plane 1.5 m × 1.5 m square at a distance of 3 m from the antenna feed point as a suitable practical specification. Overall, it was desired to obtain the largest field output whilst maintaining a uniformity of better than -6 dB between boresight and the corners of the square.

In order that the antennas could be mounted on a typical EMC height scanned mast a mass limit for each antenna of 3.5 kg was imposed.

Hyperband Antenna

The low frequency response of an antenna is principally determined by its physical size, whilst the high frequency behavior in broadband antennas is often determined by the limitations of connectors, small details of the feed, and antenna geometry leading to pattern errors and unwanted resonances. We decided to aim for an antenna with an operating frequency range of 250 MHz to 3.5 GHz though we have examined the performance up to 10 GHz where possible.

For the hyperband antenna it is expected that the shape will approximate the derivative of the exciting waveform and if the antenna has a smooth frequency response, the pulse should ideally be free of unwanted oscillatory components.

Mesoband Antennas

From the input pulse, the antenna is required to generate a damped sinusoidal ringing with a target bandwidth of ~20%. A high efficiency is desirable to produce the maximum possible pulse amplitude. As the antennas select only a limited spectral range from the broad pulse spectrum the peak fields with inevitably be smaller than from the Hyperband antenna, given the same pulse source.

III. HYPERBAND ANTENNA DESIGN

A. Antenna performance metrics

For a number of candidate antenna types the following metrics were considered for antennas of a comparable size in order to determine the most likely geometry:

- Field uniformity: This was determined as the ratio of the boresight pulse peak amplitude to the peak pulse amplitude at the corners of the specified square.
- Boresight pulse amplitude: For a unit excitation for the specified pulse, scaled to a distance of one metre from the feed point.
- Antenna mass: A maximum of 3.5 kg

B. Ridged waveguide Horn

As a ridged waveguide horn is commonly used in EMC measurements and a suitable horn was available for initial evaluation, a model of comparable size to the commercial unit was simulated using CST Microwave Studio (Fig. 2). It produced a 2.7 V/m pulse for a 1 V input pulse scaled to a distance of 1m when simulated, and had a field uniformity of

4.4 dB. The commercial antenna had a mass of more than 10 kg and a data-sheet operating frequency of 170 MHz to 3 GHz. In terms of the desired specification this would be a good antenna except for the large mass. The commercial antenna was clearly made with lightweight construction as far as possible, so we considered it unlikely that a high voltage version could be made within the desired mass limit.
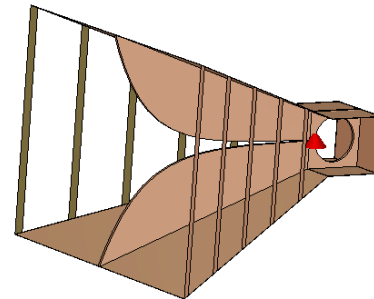
Fig. 2 932 mm×729 mm×978 mm (L×W×H) Ridged waveguide horn antenna model geometry showing excitation port (red cone)
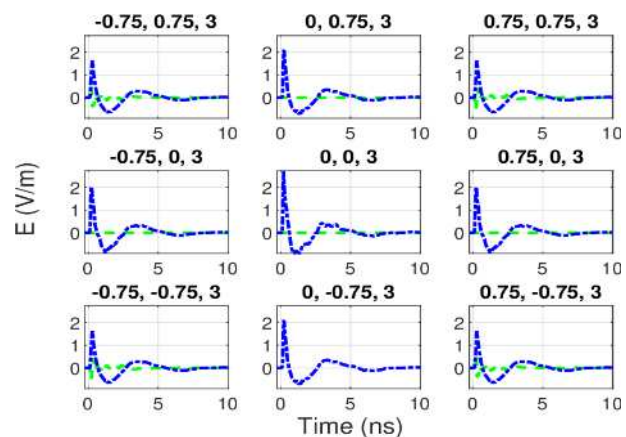
Fig. 3. Simulated pulse response of ridged waveguide horn antenna on 1.5 m × 1.5 m grid at 3 m distance from feed (probe co-ordinates with respect to feed are on top of each plot) The blue line is the co-polar field and the green line is the cross-polar field.

Fig. 3Fig. shows the simulated response of the ridged waveguide horn for the pulse specified in Section II over the 1.5 m square target areas. As expected, the pulse amplitude is reduced off-boresight and is lowest at the corners.

C. Coplanar Vivaldi Antenna

A number of other antenna types such as those cited in Section I were considered, and the coplanar Vivaldi type [15] was selected as being simple and robust to construct with a lower mass than horn types, and being planar in form, more compact than horn types.

Fig. 4 shows the geometry of a suitable prototype coplanar Vivaldi antenna. The feed distance and width were adjusted to give a 50 Ω characteristic impedance to avoid the need for a broadband impedance matching network to match the antenna

to the 50 Ω generator impedance. The inner and outer curves are exponential curves joined by a semi-circular cap. The size was chosen with the aim of achieving a similar performance to that of the ridged waveguide horn shown previously.

Fig. 5 shows the pulse response of the Coplanar Vivaldi simplified prototype antenna. Its boresight field was 2.5 V/m for a unit input pulse scaled to 1 m distance, and it had a field uniformity of 3.6 dB at the corners of the measurement plane. This corresponds to a slightly lower gain than the ridged horn antenna. The pulse exhibits less ringing and is closer to the expected derivative of the source pulse. The 8 mm antenna thickness required to achieve a 50 Ω feed impedance resulted in a mass for this antenna, of 5.8 kg without any support structure, balun, or connector, if fabricated from Aluminium. So, although the performance was promising, some further work was required to reduce the overall mass to be less than 3.5 kg.
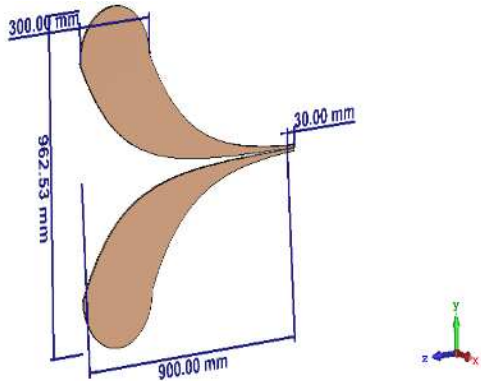
Fig. 4. 900 mm×962 mm (L× H) coplanar Vivaldi simplified prototype geometry
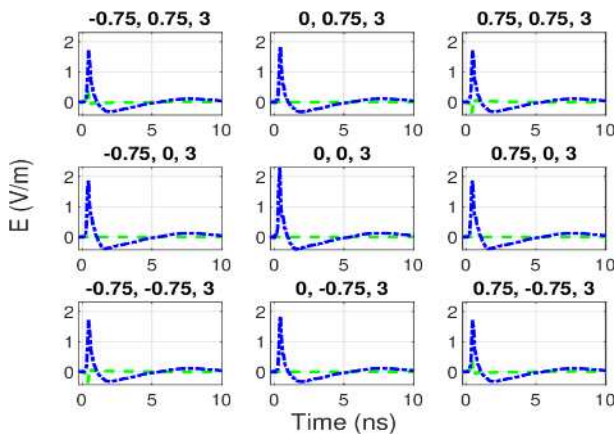
Fig. 5. Pulse response 900 mm×962 mm (L× H) Coplanar Vivaldi simplified prototype geometry (2.5 V/m at 1m for 1V pulse, -3.6 dB at corners)

D. Reduced Mass Coplanar Vivaldi antenna

In order to maintain good performance whilst reducing mass to an acceptable level a slightly smaller antenna was used in the final design as shown in Fig. 6. It has a full thickness (8mm) rim, to achieve the desired 50 Ω characteristic impedance feed,

with a thin sheet (1 mm) core away from the edges of the elements, and is made of aluminium. With the 5 mm acrylic supports used, the overall mass of the antenna was calculated to be about 2.6 kg without the balun, connector, mount and other hardware which was estimated to have a mass of 0.8 kg leading to a total mass of 3.4 kg for the finished antenna. This design when simulated had a pulse magnitude of 2 V/m for a unit pulse input scaled to 1 m distance, and a field uniformity of 2 dB at the corners of the 1.5 m square. The reduced amplitude and improved uniformity are due to the reduced size leading to its gain being slightly less than the previous, larger prototype and hence it has a broader beam.
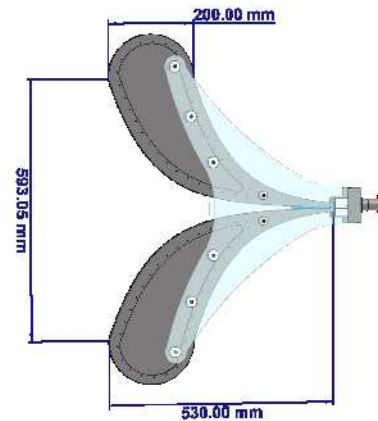
Fig. 6. 530 mm×760 mm (L× H) high voltage coplanar Vivaldi with weight reduced blades and acrylic support structure with 7-16 connector interface.

E. Connector Interface
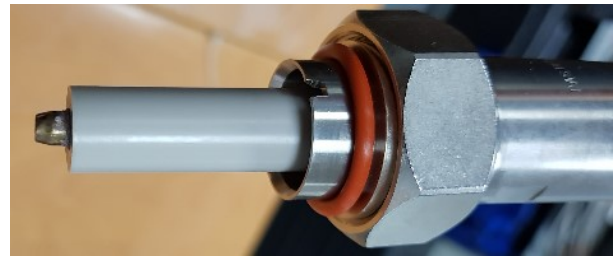
Fig. 7. Modified 7-16 plug

A modified 7-16 coaxial connector is used on the high voltage pulse generator such that the plug has an extended dielectric between the pin and outer (Fig. 7), This is so that the connector does not arc across the surface of the insulator when a high operating voltage is used. The antenna connector was manufactured as part of the antenna, using the outer and contact parts from a standard socket as can be seen in Fig. 8.

F. Transition

The coaxial input must be converted to the balanced parallel conductor transmission line that feeds the antenna. A number of solutions have been proposed in the literature such as the

Unzipper balun [16] and Klopfenstein taper [17] which provide a gradual taper from coaxial to parallel lines. To work effectively they need to be a significant fraction of a wavelength at the lowest frequency of interest. In order to ease the complexity of manufacture and minimize the length of the antenna, we experimented with a simple transition that was part of the input socket (Fig. 8). It was found to give an adequate reflection coefficient over the required frequency range of the antenna, but did not balance the feed well. The dielectric was designed to provide a large creepage distance and adequate thickness to ensure the antenna can withstand the specified voltage. In addition the feed dielectric is extended into the antenna taper for some distance, and has side plates to maintain an extended creepage distance to prevent arcing and provide a graduated transition to the air dielectric.

G. Balun

In order to achieve a good balance in the antenna feed a number of toroidal ferrites surround the feed and act as a balun, in conjunction with the transition. A small gap in each core is used to prevent the saturation of the ferrite.
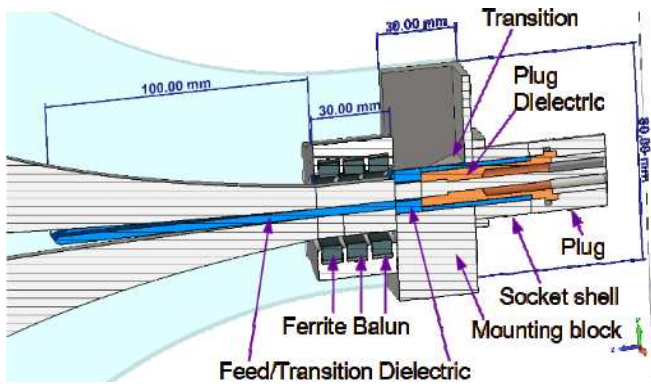
Fig. 8. Cross section through the connector transition and balun, the feed gap is 3 mm and the height of each feed bar is 8 mm. The feed dielectric is 14 mm wide and the side-cheeks have a height of 5 mm.

H. Materials

The insulator in the transition and feed was moulded from polypropylene as it has a low loss at microwave frequencies. The balun casing, and core spacers to set the gap were 3D printed using an acrylic resin as they are in an area of relatively low electric field strength, compared to the feed, and losses are less important than ease of manufacture here. The transition was made from aluminium, and designed to mate with parts from a disassembled, off-the-shelf, socket.

IV. 150 MHz Mesoband Antenna Design

This mesoband antenna is intended to produce a damped sinusoid at 150 MHz in response to the input pulse. Previously it was common to use a dipole antenna with an inbuilt spark

gap, to generate damped sinusoidal pulses of high amplitude.

Antenna prototyping was carried out using the time-domain full wave solver from the CST Microwave Studio Suite. Whilst a simple dipole has the required characteristics, we found that a kite-shaped element (Fig. 9) had more scope for bandwidth control by adjustment of the shape, better suppression of higher order resonances (Fig. 10) and an input impedance closer to the desired 50 ohms than a simple dipole.
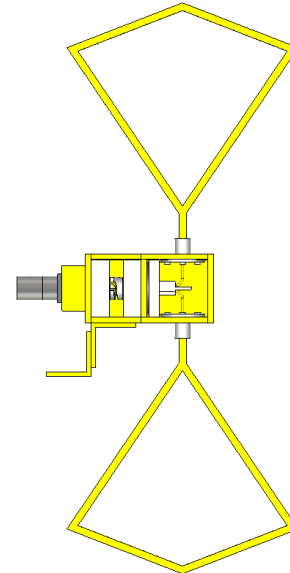
Fig. 9. Kite shaped high-voltage mesoband dipole, with enclosure lid removed, showing integrated filter (left cavity) and balun (right cavity)
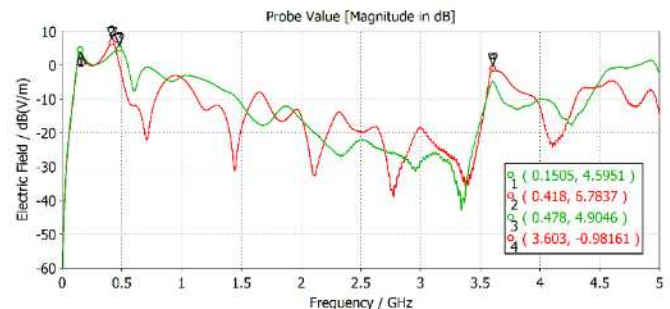
Fig. 10. Modelled boresite field at 4 m for unit excitation (green) compared with simple dipole (red)

A. Connector Interface and low pass filter

The same modified 7-16 coaxial connector is used as the Hyperband antenna and the socket is built into the antenna with 3D printed dielectric parts in conjunction with the metal parts from a dismantled off-the-shelf connector.

Although the kite element chosen gives some suppression of the second antenna resonance that occurs around 500 MHz (Fig. 10) there is still much energy in the exciting pulse at that frequency, so we decided to add a 3 element pi-type low-pass filter to further suppress higher order resonances. The connector interface and low pass filter can be seen in cross-section in Fig.

11. The filter capacitors consist of a metal plate separated from the enclosure wall by a 3D printed dielectric. The input capacitor is connected directly to the socket receptacle of the plug. The inductor is wound on a 3D printed former and the output capacitor is connected directly to the balun though a feedthrough in the enclosure divider. The output capacitor of the filter also performs a matching function to remove the reactive part of the impedance seen at the input of the balun.
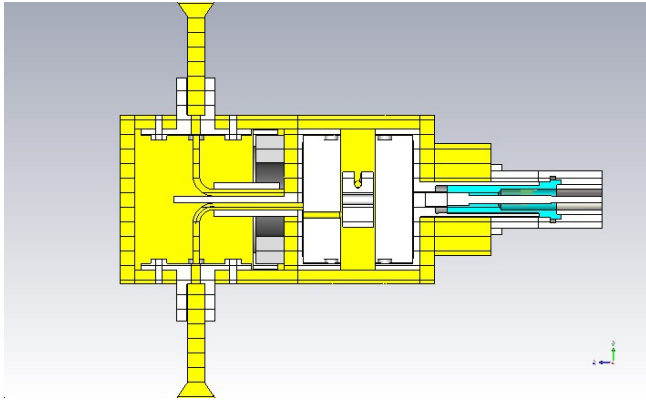
Fig. 11. Cross section of connector transition, low-pass filter and balun

B. Balun

In order to achieve a good balance in the antenna feed a single ferrite core is used. A small gap is used to prevent the saturation of the ferrite. The layout of the balun can be seen in cross-section in Fig. 11. The modelled input impedance of the antenna with filter and balun can be seen in Fig. 12. It shows a good match around 150 MHz (Marker 1).
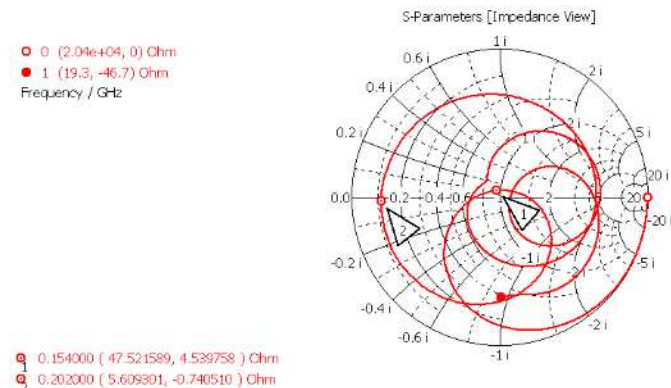
Fig. 12. Modelled complex impedance at the balun input for the antenna at 154 MHz (marker 1) and 202 MHz (marker 2)

C. Materials

The antenna balun and filter enclosure, and arms were fabricated from aluminium, the insulators were 3D printed from an acrylic resin, whilst the filter and balun wires are copper. The filter capacitor plates were fabricated from brass sheet. As the complex permittivity of the acrylic resin is not specified by the manufacturers, we measured a 3D printed sphere using the resonance perturbation technique described in [18] where it was

found to be 2.94-j0.699 at 437 MHz. This is somewhat higher than data for standard acrylic material (plexiglass) as measured in [19].
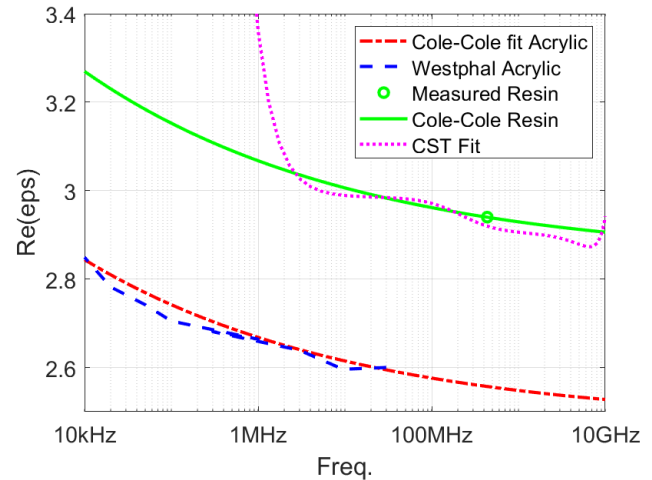
Fig. 13. Comparing the measured and estimated real part of the permittivity of the acrylic resin with plexiglass acrylic as measured in [19]
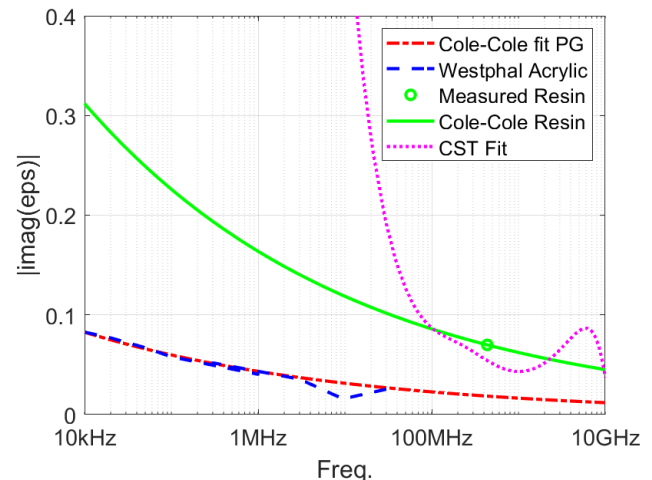
Fig. 14. Comparing the measured and estimated imaginary part of the permittivity of the acrylic resin with plexiglass acrylic as measured in [19]

We fitted a Cole-Cole model [20] to the data from [19] and scaled the curve to fit our measured value for the resin as shown in Fig. 13 and Fig. 14. However, the CST simulator does not implement the Cole-Cole model and therefore the final values used in the simulator material model were chosen to approximate the Cole-Cole model in the main operating frequency range which can also be seen in the figures.

V. 1.3 GHz MESOBAND ANTENNA DESIGN

From the input pulse, it was desired that the antenna generate a damped mesoband oscillation with a target bandwidth of 10% to 30%. A high efficiency is required to produce the maximum

possible pulse amplitude. Since the energy in the pulse falls with frequency a smaller field is expected, compared with the 150 MHz antenna.

Manual optimisation of the antenna was carried out using the CST Microwave Studio time domain solver. Fig. 15 shows the simulation CAD model for the complete design with the cover removed. In simulation the source excitation is applied to a short section of coaxial cable prior to the connector interface. Due to the requirement to interface to a modified, high voltage 7-16 coaxial connector, the case size was comparable to the dipole and we found it was necessary to use a reflector to control the interaction between the case and antenna. In order to withstand the high voltage; and allow matching and low pass filtering of the input pulse to be carried out with transmission line elements, a double thickness PCB of standard FR4 laminate was used to fabricate the antenna, balun, filter and matching network. Parts from a standard connector along with a moulded polypropylene insulator were used to fabricate the connector interface which incorporates a compact transition from the coaxial connector to the stripline transmission line on the PCB.

The metal parts were machined from aluminium. The insulator where the antenna leaves the case and the spacers to set the gap in the balun ferrite core were 3D printed using an acrylic resin as they are in an area of low electric field strength and losses are less important, than ease of manufacture.
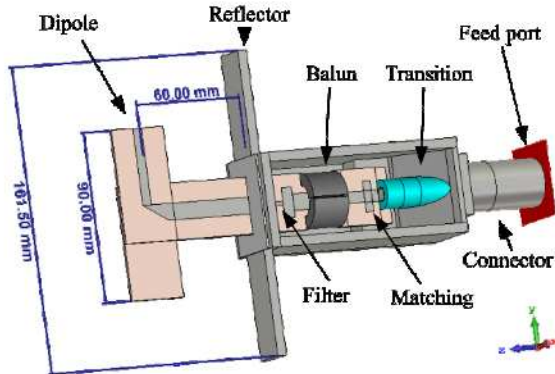
Fig. 15 View of simulation CAD model of 1.3GHz mesoband high voltage dipole with enclosure lid removed showing balun, filter and matching.

A. Connector interface

The transition from the coaxial 7-16 connector (Fig. 7) to a PCB microstrip line was achieved by tapering the outer of the socket interface quite rapidly about the plug; attaching the centre conductor socket directly to the PCB, and sitting the PCB ground-plane on a step in the connector interface block, as shown in Fig. 16. It achieved a reflection coefficient of better than -15 dB up to about 1.5 GHz in a 50 Ω system. An open circuit matching stub is included in the stripline to achieve this.
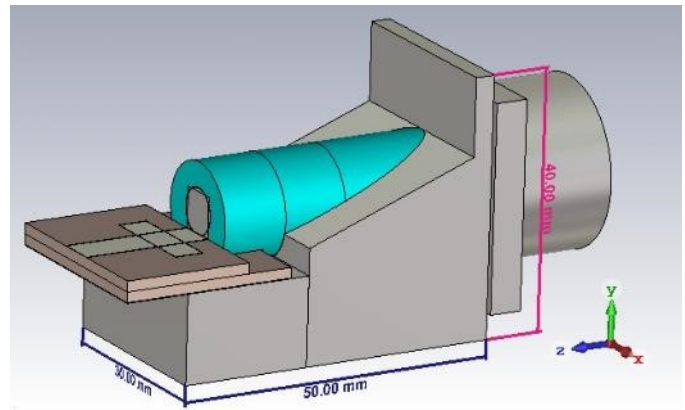
Fig. 16. Connector interface and transition to stripline with open circuit matching stub.

B. Balun and Low pass filter

The balanced stripline follows the connector interface with a simple step transition between the two lines. Initially we thought that the balanced line might be sufficiently well coupled to balance the antenna with no magnetic components, but we found a longitudinal common mode resonance in the feed causing it to radiate rather like a top-hat dipole at 430 MHz (Fig. 17). The addition of the gapped ferrite core, both reduced the top-hat resonance to negligible proportions and improved the balance at the desired frequency.

As the boresight field from the antenna showed a strong higher order resonance at about 3.6 GHz (Fig. 18) a 3rd order low pass transmission line filter was incorporated after the balun to provide about 8 dB of suppression at 3.6 GHz. As the spectrum of the pulse has a low pass characteristic further reduction of higher order resonances is achieved.
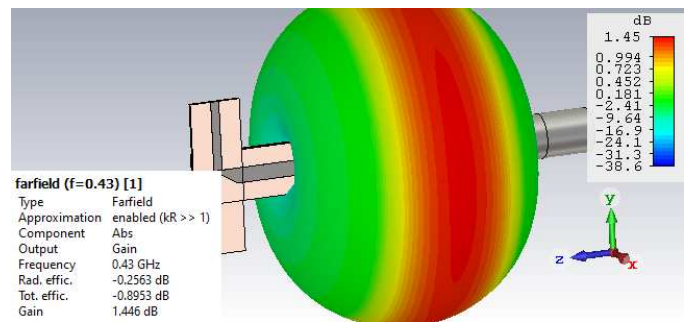
Fig. 17. Top-hat radiation mode at 430 MHz, without ferrite in balun .
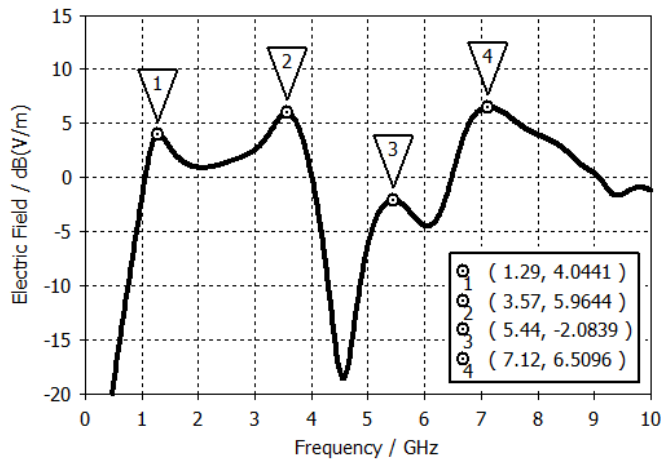
Fig. 18. Boresight frequency response of antenna without filter, at 4 m for 1 V excitation.

C. Reflector

Due to the large size of the modified 7-16 high voltage connector the case height is necessarily quite large compared to the overall size of the dipole and we found that it distorted the dipole pattern as shown in Fig. 19. To solve this and increase the gain we decided to add a reflector to the case as can be seen in Fig. 15.
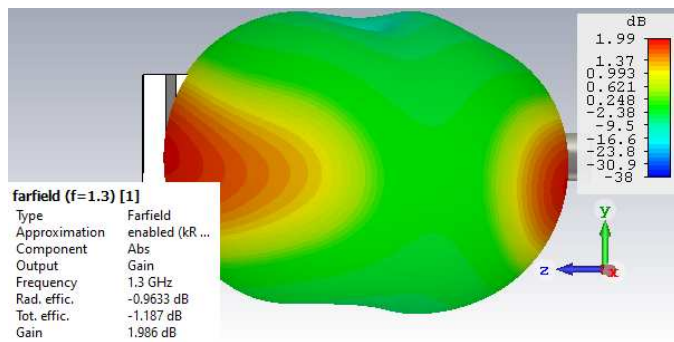
Fig. 19. Effect of case on radiation pattern with no reflector at 1.3GHz
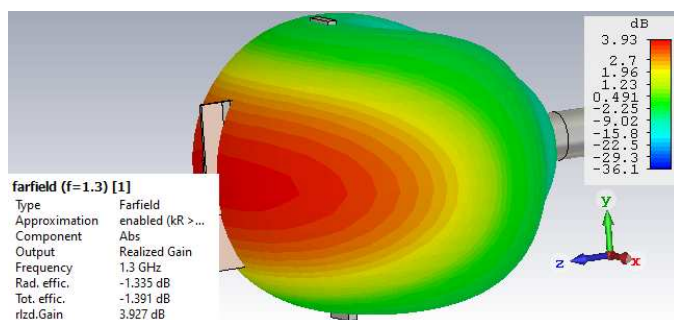
Fig. 20. Radiation pattern with reflector at 1.3 GHz.

Fig. 20 shows the modelled radiation pattern with the reflector present. It can be seen that the realised boresight gain is increased to 3.9 dB compared with the 1.8 dB modelled value

for the simple PCB dipole with no feed or case.

VI. Measurement Setup and procedure

The performance of the three antennas was measured in an anechoic chamber using both a vector network analyser (VNA) in the frequency domain and in the time domain by means of a high voltage pulse generator and sampling oscilloscope. The frequency domain results were obtained from 10 MHz to 10 GHz and the time domain results were obtained with a 20 G/sample/s oscilloscope with a nominal 2.5 GHz bandwidth. The equipment is housed outside the chamber and fed through a penetration panel. The measurements were carried out using a D-dot sensor to measure the field produced by the antenna. The D-dot sensor was placed at 9-positions on a plane at 3 m from the antenna feed point. One position was centered on the antenna boresight with the other 8 at positions $\pm$1.5 m either side of and up and down from the boresight position.

In the case of the frequency domain measurements it was only possible to calibrate the VNA to the end of the N-type bulkhead adaptor to which the 3 m antenna cable with modified 7-16 connector was connected. The other port was calibrated at the end of the cable connected to the D-dot sensor. Allowance for the loss of the antenna cable was made in the data processing.

In the case of the time domain measurements we had no capability to measure the high voltage excitation and so the ideal waveform was assumed. Again allowance for the loss of the antenna cable was made in the data processing.

Fig. 21. Hyperband antenna under test (right) in anechoic chamber, showing D-dot probe (left)

VII. Data processing

Cable loss

The cable loss in dB/m for the antenna feed cable was approximated in the frequency domain from generic data for RG217 cable [21]. Dispersion was ignored. The cable transmission coefficient, H_C was then computed for the 3 m cable for use in later processing.
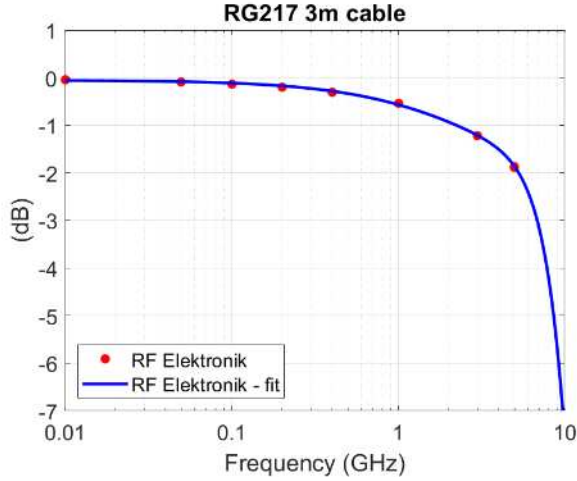
Fig. 22. Cable loss model based on fitting a polynomial to generic loss data.

D-dot sensor and balun

A D-dot sensor [22] with a BL3-5G Ultra Broadband balun was used for all field measurements. The response of the D-dot sensor is defined in the Laplace domain as [23]:

$$V_D(s) = A \frac{sR}{1+sRC} \epsilon_0 E(s) \qquad (2)$$

where $V_D(s)$ is the voltage developed across the load resistance $R = 50\ \Omega$; $A = 2 \times 10^{-3}\ \mathrm{m}^2$ is the equivalent area of the sensor; C is the capacitance of the sensor; $E(s)$ is the incident electric field parallel to the axis of the sensor, and ϵ_0 is the permittivity of free-space. The capacitance can be computed from the given -3 dB frequency: $f_{0D} = 3.5$ GHz:

$$f_{0D} = \frac{1}{2\pi RC} \rightarrow C = \frac{1}{2\pi R f_{0D}} \qquad (3)$$

The received E-field can be written as:

$$E(s) = \frac{1}{A\epsilon_0} \cdot \frac{1+sRC}{sR} V_D(s) \qquad (4)$$

Therefore, the Antenna factor, such that $E(s) = V_D(s)F_D(s)$, of the probe is:

$$F_D(s) = \frac{1}{A\epsilon_0} \cdot \frac{1+sRC}{sR} \qquad (5)$$

and the frequency response of the probe may be written as:

$$H_D(s) = \frac{V_D(s)}{E(s)} = A \frac{sR}{1+sRC} \epsilon_0 = \frac{1}{F_D(s)} \qquad (6)$$

The balun has a nominal loss of $L_B = 6.2$ dB and an upper -3dB frequency of $f_{0B} = 3.5$ GHz. In the absence of any other detail, we model this as a second order Butterworth low-pass response:

$$H_B(s) = \frac{10^{\left(-\frac{L_B}{20}\right)}}{1+\left(\frac{s}{2*\pi*f_{0B}}\right)^2} \qquad (7)$$
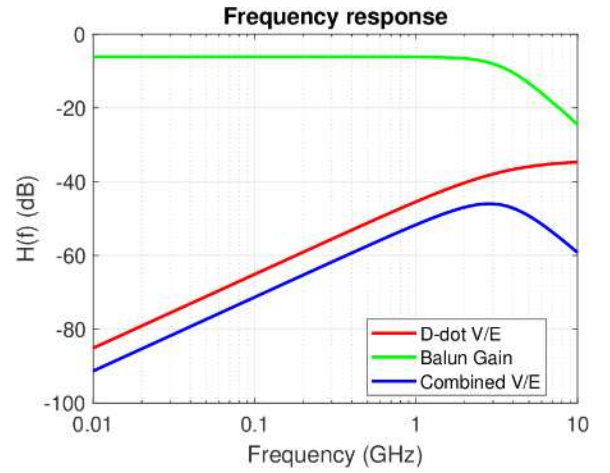
Fig. 23. Frequency response of D-dot sensor and Balun

Chamber and cable effects

To establish the effect of chamber imperfections on the measurements each set was conducted with vertical and horizontal polarisation, as any difference in performance observed must be due to the chamber and/or cables rather than the antenna.

Frequency domain

Measurements were taken from 10 MHz to 10 GHz in 1 MHz steps and the transmission between the antenna and sensor was negligible below 10 MHz.

The antenna E-field, scaled to, 1 m was therefore computed from the transmission (S_{21}) between the antenna cable input and the D-dot sensor balun output as:

$$E_0(s) = \frac{dS_{21}(s)}{H_D(s)H_B(s)H_C(s)} \qquad (8)$$

where d is the measurement distance.

The time domain field can be calculated by multiplying the E-field spectrum by the pulse spectrum and performing an inverse Fast Fourier Transform (FFT) on the data.

Time domain

In order to remove the effects of the antenna cable losses, balun, the time data was converted into the frequency domain, and processed as in (8). As the oscilloscope used had a low pass anti-aliasing filter with a maximally flat (Butterworth) frequency response, and by comparing the measured VNA data with that from the pulse source we were able to deduce that the response is that of a 4th order Butterworth filter with a cutoff frequency of 1.1 times the nominal 2.5 GHz oscilloscope bandwidth. So, in order to extend, a little, the spectrum of the time-domain data beyond the nominal 2.5 GHz oscilloscope bandwidth we also applied a band-limited inverse filter to the time domain data. In addition the spectra of the pulses were averaged over 1024 measurements to reduce the noise floor, and increase the resolution of the measurement.

VIII.   MEASURED AND MODELLED PERFORMANCE COMPARISON

Hyperband antenna

The reflection coefficient of the antenna is shown in Fig. 24. Initial VNA measurements at the UoY (light blue), are compared with VNA measurements in QinetiQ's laboratory (red), and the results of the numerical simulation (green). It can be seen that the actual antenna does not perform quite as well as the model, but a useable reflection coefficient around -8 dB is achieved over the operating band. The measurements at QinetiQ's laboratory show periodic oscillations thought to be due to cable/connector imperfections.
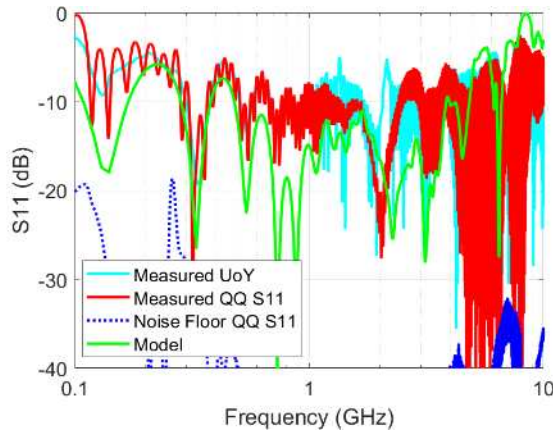
Fig. 24. Comparing the measured and simulated reflection coefficient

Fig. 25 shows the received pulse scaled to 1 V excitation and 1 m distance. For the frequency domain vertically polarised measurement (VNA V) with a VNA the pulse response is obtained from the inverse FFT of the transmission measurement convolved with the expected source pulse. The limited oscilloscope bandwidth is expected to result in a reduced amplitude of the measured pulse and our prediction is given as VNA VS. Two pulse measurements are shown with the antenna in vertical (6kV V 0dB) and horizontal (6kV H 0dB) polarisations. In all cases the measurements are adjusted for D-dot, balun, and cable losses. The pulses are offset in time to allow the initial peak to be clearly seen.
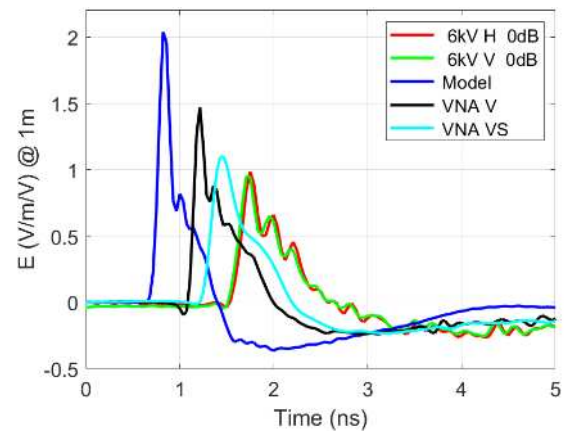
Fig. 25. Comparing boresite pulse from numerical model with VNA and pulse measurement. Pulses are offset in time so peaks can be seen clearly.

The VNA measurements show a smaller pulse than was predicted by the numerical model. We believe this is due to the imperfection of the model and small differences between the model and built antenna resulting in reduced gain. Also, some difference may be due to uncertainty in the balun, and cable parameters. It can also be seen that the time domain measurements show a smaller pulse than expected based on the VNA measurements. We think this is due to the uncertainty in the amplitude and shape of the pulse generator waveform. However, as we were unable to measure the pulse directly this cannot be verified.
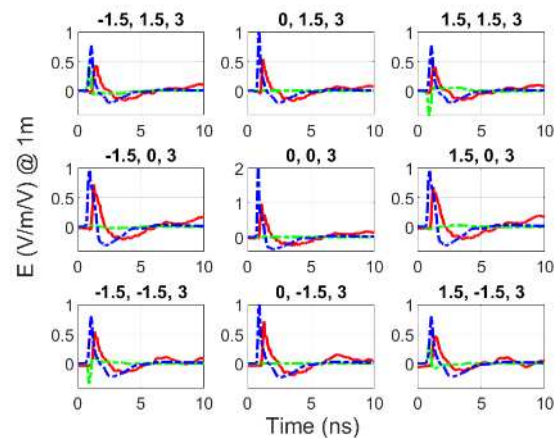
Fig. 26. Comparing the pulse shapes over a 3 m × 3 m grid (vertical polarisation). Red: measured; blue dashed: Model co-polar; green: model cross-polar. Pulses are offset in time so peaks can be seen clearly.

Fig. 26 shows the simulated and measured pulse shapes in the centre and along the edges of a 3m square measurement grid. It can be seen that although the boresight pulse amplitude is lower (0.95 V/m/V) than predicted by the simulation (2 V/m/V) the reduction in the field at the corners is less in the measurement (-7.4 dB) than predicted by the simulation (-8.5 dB) suggesting that the gain is lower than predicted by the

model. This correlates with the reduced gain seen in the frequency domain and is part of the reason for the lower than predicted boresight pulse amplitudes seen.
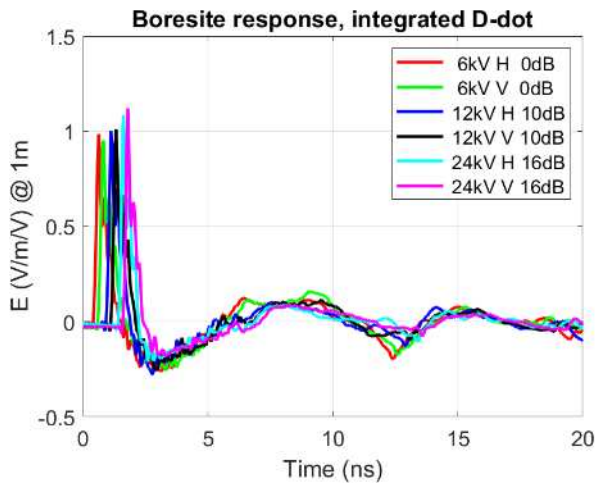
Fig. 27. Effect of pulse amplitude on pulse shape – all pulses are scaled to field at 1 m for a 1 V pulse. The attenuation used before the oscilloscope is shown on the key and compensated for in the calculation, so all pulses should be equal in amplitude.

In order to test the high voltage capability of the antenna the output pulse was measured. The results for 3 amplitudes for both horizontal and vertical polarisations can be seen in Fig. 27. Whilst there is some small difference in the late time response and normalised amplitude, we believe this to be due to the uncertainty in the generator output. Any arcing within the antenna would show as a change in pulse shape. We observed there to be little difference over the 1024 pulses recorded. If arcing was occurring, one would expect a change in shape with time as the arc occurred.

150 MHz mesoband antenna

The antenna simulated reflection coefficient, is compared with that measured at the University of York and QinetiQ's laboratories in Fig. 28. The measurements show some periodic oscillations thought to be due to cable/connector imperfections. Also we note that the reflection coefficient minima above 1 GHz, due to higher order resonances, differ in detail. We believe this is due to small differences between the model and built antenna geometry. Also there are some additional oscillations in the measurements at QinetiQ's laboratory which we think are due to connector or cable imperfections. Overall, the antenna shows a reflection coefficient of better than -8dB across its operating bandwidth and a high, close-to-zero decibel reflection coefficient elsewhere, as desired to minimise out of band radiation influencing the pulse shape.
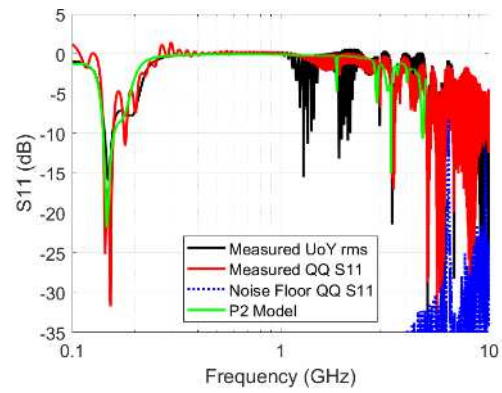
Fig. 28. Comparing measured and simulated reflection coefficient

Fig. 29 shows the antenna and pulse generator under test in QinetiQ's anechoic chamber configured for horizontal polarisation.

Fig. 29. 150 MHz Antenna under test in anechoic chamber with pulse generator below

Fig. 30 shows the received pulse scaled to 1 V excitation and 1 m distance. For the frequency domain vertical and horizontal polarisation measurements with a VNA (VNA V, and VNA H) the pulse response is obtained from the inverse FFT of the transmission measurement convolved with the expected source pulse. The pulsed measurements were taken with a 6 kV pulse (6kV H and 6kV V). In all cases the measurements are adjusted for D-dot cable and cable losses and oscilloscope bandwidth, the pulses are offset in time to allow the initial peak to be clearly seen. Both horizontal and vertical polarisation measurements were performed to reveal any chamber or cable effects on the measurement. The initial cycle of oscillation corresponds well in all cases. The later cycles diverge a little from the model with a slower decay. Also, some difference can be seen between the horizontal and vertical pulsed measurements which is not apparent with the VNA measurement. As can be seen in Fig. 29, the pulse generator was placed under the antenna for pulsed measurements whereas it was not present during VNA measurements, the antenna cable was run away from the

antenna for about 1m before the vertical drop in both cases. In the VNA measurements it then ran across the chamber floor and up to the connector panel at the other end of the chamber. We therefore suspect the presence of the pulse generator to be the cause of the differences in horizontal and vertical measurements in the pulsed case.
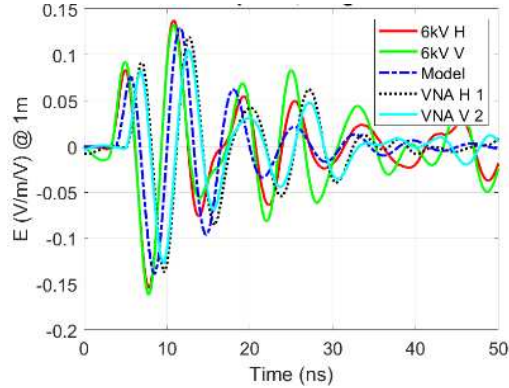
Fig. 30. Comparing boresite pulse from numerical model with VNA and pulse measurement. Pulses are offset in time so peaks can be seen clearly.

Fig. 31 shows the simulated and measured pulse shapes over a 3 m square measurement grid. It can be seen that the model results correspond well with the measured data.
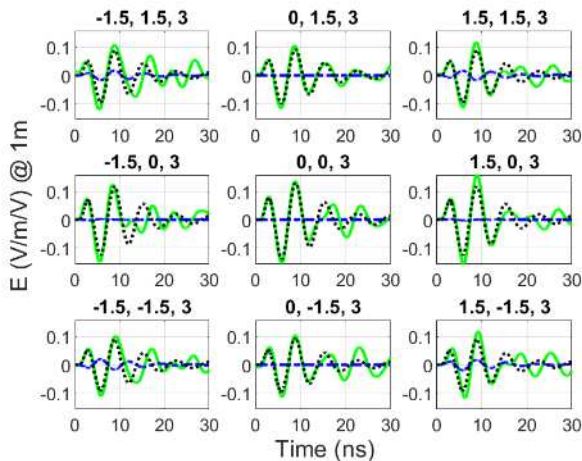
Fig. 31. Comparing the pulse shapes over a 3 m × 3 m grid (vertical polarization). Green: measured; black dashed: Model co-polar; blue: model cross-polar. Pulses are offset in time so peaks can be seen clearly.

Successful operation with a 24 kV input was established by looking for any change in the pulse shape over the sequence of 1024 pulses with a 24 kV excitation. Any arcing within the antenna would affect the shape of the pulse. Fig. 32 shows variation over 1024 pulses by plotting the mean, maximum and minimum values. The small variation seen appears to be due to the variation in the oscilloscope trigger point.
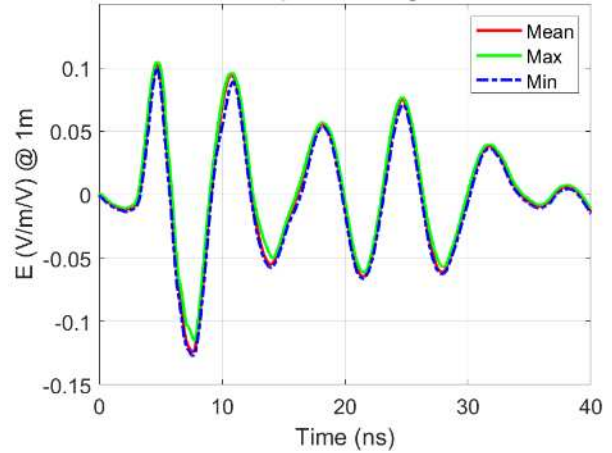
Fig. 32. Envelope of 1024 pulses for 24 kV input amplitude

1.3 GHz mesoband antenna

Fig. 33 shows the simulated and measured antenna reflection coefficients which are in good agreement, and a reflection coefficient of better than -10 dB is achieved over the operating band.
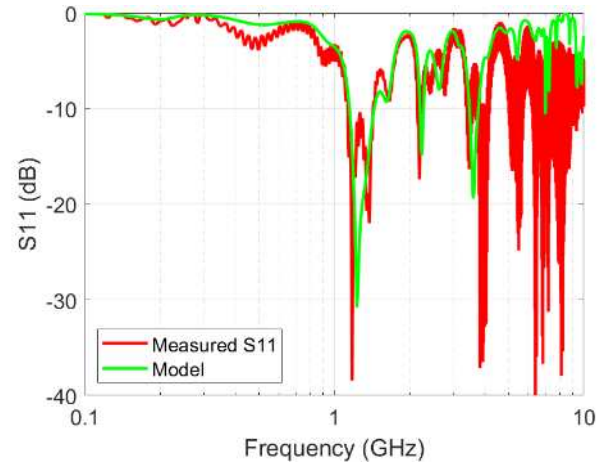
Fig. 33. Comparing the measured and simulated reflection coefficient
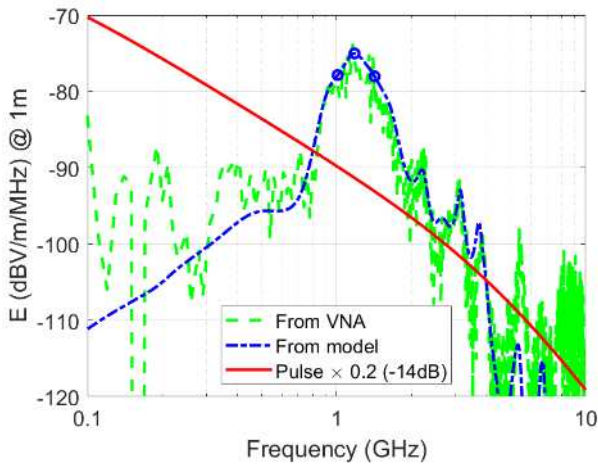
Fig. 34. Comparing simulated and measured (VNA) boresight pulse spectrum from the antenna along with the input pulse spectrum scaled to the same amplitude range, for a unit pulse. Circles show max and -3 dB bandwidth limits.

Fig. 34 shows the pulse spectrum simulated and determined from VNA measurements multiplied by the spectrum of the ideal pulse, along with the input pulse spectrum.
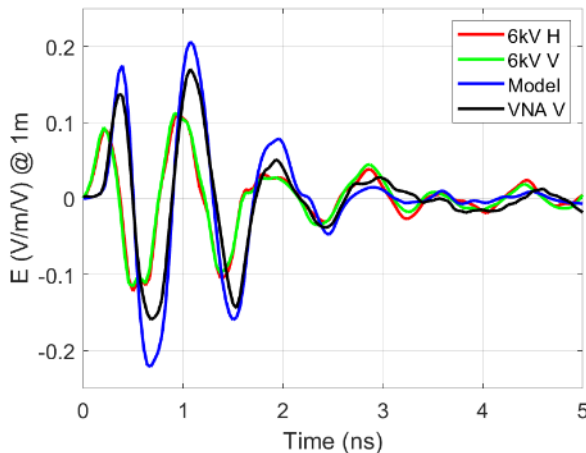
Fig. 35. Comparing antenna boresight numerical model results with VNA and pulse measurement – all pulses are scaled to field at 1 m for a 1 V pulse

The received pulse scaled to 1 V excitation and 1 m distance is shown in Fig. 35. For the frequency domain measurement (VNA V) with a VNA the pulse response is obtained from the inverse FFT of the transmission measurement convolved with the expected source pulse. Two measurements are shown with the pulse generator with the antenna and D-dot sensor in vertical (6kV V) and horizontal orientations (6kV H) in the chamber, any difference might be attributed to the chamber. In all cases the measurements are adjusted for D-dot, balun, and cable losses, the pulses are offset in time to allow the initial peak to be clearly seen.

The simulated and measured pulse shapes over a 3 m square measurement grid can be seen in Fig. 36. The numbers at the

top of each plot show the x, y and z co-ordinates of the measurement grid relative to the antenna. It can be seen that although the boresight pulse amplitude is lower than predicted by the simulation, the reduction in the field at the corners is less in the measurement, suggesting that the gain is lower than predicted by the model.

Fig. 37 shows the measured pulse for different source voltages for both horizontal and vertical antenna orientations. Two antenna orientations are used to determine if the chamber causes any features in the waveform due to reflections. Some small differences can be seen in the late-time response when the antenna is switched between the two orientations which we believe is due to chamber reflections. All the pulses are scaled to a unit excitation and a distance of 1m.
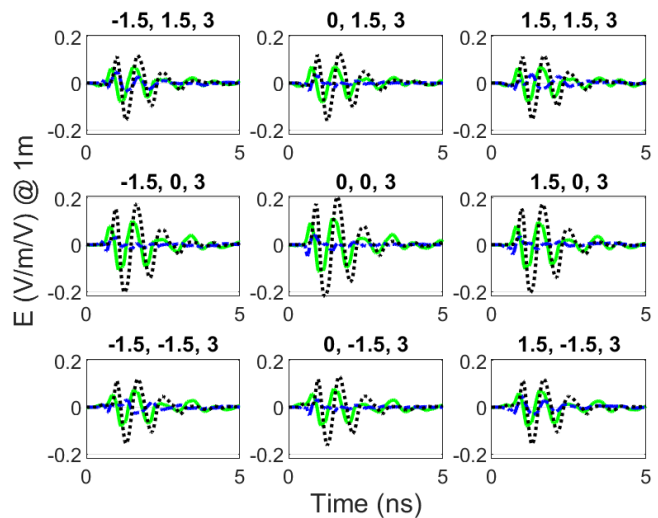
Fig. 36. Comparing the pulse shapes over a 3 m × 3 m grid (vertical polarization) in a plane 3 m from antenna. Green: measured; black dashed: Model co-polar; blue: model cross-polar. Pulses are offset in time so peaks can be seen clearly and scaled to 1 m distance.
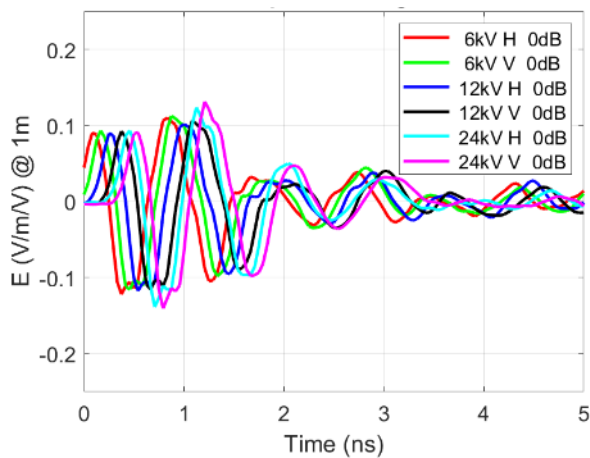
Fig. 37. Effect of boresight pulse amplitude on pulse shape – all pulses are scaled to field at 1 m for a 1 V pulse, H and V designates horizontal and vertical antenna orientations respectively

IX. Conclusions

We have demonstrated that it is possible to produce hyperband and mesoband pulses using a single pulse source driving tuned antennas with suitable low pass filtering, and a broadband antenna. We have also managed to produce a broadband antenna of robust construction but light enough to be used with a standard EMC test mast. All the antennas achieve a good uniformity of amplitude and pulse shape over a 3 m square. The system is intended for use in IEMI susceptibility testing of equipment.

The antennas were designed using computational modelling and the realised performance of the fabricated antennas is close to that predicted by the modelling.

The principal challenges in producing the antennas were in determining the dielectric performance of the materials available for use and being able to produce a design that can be machined and fabricated without loss of performance.

Acknowledgment

References

[1] *BS IEC 61000-4-36:2020 Electromagnetic compatibility (EMC). Testing and measurement techniques. IEMI immunity test methods for equipment and systems*. 2020, Available: https://bsol.bsigroup.com/Bibliographic/BibliographicInfoData/0000 00000030355559.

[2] *Protection Against Interference, 'High-power electromagnetic immunity guide for telecommunication systems*, no. ITU-T K.81, SERIES K: 2009.

[3] *Electromagnetic Environmental Effects, Requirements for Systems*, no. Mil-Std-464C. 2010.

[4] W. A. Radasky and M. W. Wik, "Overview of the threat of intentional electromagnetic interference (IEMI)," in *2003 IEEE International Symposium on Electromagnetic Compatibility, 2003. EMC '03.*, 2003, vol. 2, pp. 1024–1027 Vol.2.

[5] P. Angskog, P. Nasman, and L. G. Mattsson, "Resilience to Intentional Electromagnetic Interference Is Required for Connected Autonomous Vehicles," *IEEE Transactions on Electromagnetic Compatibility*, vol. 61, no. 5, pp. 1552–1559, 2019, Available: <Go to ISI>://WOS:000498690200018.

[6] C. E. Baum, E. G. Farr, and D. V. Giri, "Review of impulse-radiating antennas," *Review of Radio Science*, pp. 403–439, 1999.

[7] J.-. Diot, P. Delmote, J. Andrieu, M. Lalande, V. Bertrand, B. Jecko, S. Colson, R. Guillerey, and M. Brishoual, "A Novel Antenna for Transient Applications in the Frequency Band 300 MHz – 3 GHz: The Valentine Antenna," *IEEE Transactions on Antennas and Propagation*, vol. 55, no. 3, pp. 987–990, Mar. 2007.

[8] J. S. Kim, Y. Yoon, H. Kwon, J. Ryu, and J. S. Choi, "A Directive Subminiature Antenna for High-Power Ultrawideband Pulse Radiation," *IEEE Antennas and Wireless Propagation Letters*, vol. 13, pp. 1565–1568, 2014.

[9] X. Li, S. C. Hagness, M. K. Choi, and D. W. van der Weide, "Numerical and experimental investigation of an ultrawideband ridged pyramidal horn antenna with curved launching plane for pulse radiation," *IEEE Antennas and Wireless Propagation Letters*, vol. 2, pp. 259–262, 2003.

[10] H. Park, J. Kim, J. Ryu, J. Choi, and Y. Yoon, "Modified low-frequency compensated TEM (LFCTEM) horn antenna to improve the radiation performance," in *2013 Asia-Pacific Microwave Conference Proceedings (APMC)*, 2013, pp. 1163–1165.

[11] J. Schmitz, M. Camp, M. Jung, G. Adamiuk, S. Scherr, and T. Zwick, "UWB Dual-Polarized Antenna for HPEM Sources," in *Ultra-Wideband, Short-Pulse Electromagnetics 10*, 2014, pp. 189–197.

[12] S. Wang and Y. Xie, "Design and Optimization of High-Power UWB Combined Antenna Based on Klopfenstein Impedance Taper," *IEEE Transactions on Antennas and Propagation*, vol. 65, no. 12, pp. 6960–6967, Dec. 2017.

[13] R. Hoad, L. Chatt, B. Petit, T. Rees, and G. Eastwood, "Mesoband and Hyperband Immunity Test Generator and Standards," in *AMEREM*, 2018, Available: http://ece-events.unm.edu/amerem2018/program/_program.html.

[14] G. Wu, "Shape Properties of Pulses Described by Double Exponential Function and Its Modified Forms," *IEEE Transactions on Electromagnetic Compatibility*, vol. 56, no. 4, pp. 923–931, Aug. 2014.

[15] P. J. Gibson, "The Vivaldi Aerial," in *Microwave Conference, 1979. 9th European*, 1979, pp. 101–105.

[16] E. G. Farr, Gary D. Sower, and C. J. Buchenauer, "Design Considerations for Ultra-Wideband, High-Voltage Baluns," FARR RESEARCH ALBUQUERQUE NM, 1994, Available: http://www.dtic.mil/docs/citations/ADA332114.

[17] R. W. Klopfenstein, "A Transmission Line Taper of Improved Design," *Proceedings of the IRE*, vol. 44, no. 1, pp. 31–35, Jan. 1956.

[18] M. Robinson, L. Fitton, A. Little, S. Cobb, and D. S. Ashby, "Dielectric Replica Measurement: A New Technique for Obtaining the Complex Permittivity of Irregularly Shaped Objects," *Meas. Sci. Technol.*, 2019.

[19] W. B. Westphal, "Dielectric Constant and Loss Data. Part 4," MASSACHUSETTS INST OF TECH CAMBRIDGE LAB FOR INSULATION RESEARCH, Dec. 1980, Available: http://www.dtic.mil/docs/citations/ADA121008.

[20] K. S. Cole and R. H. Cole, "Dispersion and Absorption in Dielectrics I. Alternating Current Characteristics," *The Journal of Chemical Physics*, vol. 9, no. 4, pp. 341–351, 1941.

[21] "Coaxial Cable Attenuation Charts", Available: http://rfelektronik.se/manuals/Datasheets/Coaxial_Cable_Attenuation_Chart.pdf.

[22] "Electromagnetic Free Field Sensors Data sheet," Montenna, Available: https://www.montena.com/fileadmin/technology_tests/documents/data_sheets/Data_sheet_SF_free_field_sensors.pdf.

[23] S. L. Olsen, "Asymptotic Conical Dipole D-Dot Sensor (ACD-S1 (R)) Development," 1976, Available: http://www.dtic.mil/docs/citations/ADA039657.

John F. Dawson (Member, IEEE), received his BSc and DPhil degrees in Electronics from the University of York, U.K., in 1982 and 1989. He is currently a Senior Lecturer at the University of York. His research interests include: reverberation chamber techniques, shielding, numerical modelling, EMC for circuits and systems.

Simon J. Bale (Member, IEEE), received the M.Eng. and Ph.D. degrees in electronics from the University of York, U.K., in 2004 and 2012. He is currently a Senior Lecturer at the University of York. His research interests include: His current research interests include oscillators and atomic clocks; EMC and shielding; and microelectronic design optimisation using bio-inspired methods and techniques.

Martin P. Robinson, received the B.A. and M.A. degrees from the University of Cambridge, Cambridge, U.K., in 1986 and 1990, respectively, the M.Sc. degree in medical physics from the University of Aberdeen, U.K., in 1990, and the Ph.D. degree in dielectric imaging from the University of Bristol, U.K., in 1994. He is currently a Senior Lecturer in the Communication Technologies Group at York, doing research in Applied Electromagnetics and teaching at undergraduate and postgraduate level. His current research interests include electromagnetic compatibility and shielding, as well as applying microwave and radio frequency techniques to a wide range of problems, such as medical diagnosis and therapy, environmental sensing of pollutants and object identification in archaeology. He has served on various special interest groups and committees of IPEM, IoP and URSI.

Tim Rees, photograph and biography not available at the time of publication.

Barnabas J. Petit (Member IEEE), received his MEng in Electrical and Electronic Engineering from the University of Bath in 2006. He is a Senior Principal Scientist at QinetiQ Ltd, with interests in high power microwaves, radio frequency directed energy systems, and wireless power transfer.

Richard Hoad (Senior Member IEEE), Chief Engineer and Capability Area Leader for Directed Energy and Weapons Systems at QinetiQ Ltd. In his role as capability area leader Richard provides strategic oversight and leadership of QinetiQ's capability; defined as people/skills, facilities, partnerships and intellectual property (IP), in High Power Radio Frequency (HPRF); High Energy Laser (HEL); and other directed energy technologies.

Mark Hough, received a Higher National Certificate in electronics and communications engineering from York Technical College in 1990. He is Chief Technician in the School of Physics, Engineering and Technology, and a specialist in mechanical CAD, CNC and 3D-printed fabrication.